

# Rock Cavern Stability Analysis Under Different Hydro-Geological Conditions Using the Coupled Hydro-Mechanical Model

H. M. Chen<sup>1</sup> · Z. Y. Zhao<sup>1</sup> · L. Q. Choo<sup>1</sup> · J. P. Sun<sup>2</sup>

Received: 26 March 2014 / Accepted: 31 March 2015 / Published online: 1 May 2015  
© Springer-Verlag Wien 2015

**Abstract** Rock cavern stability has a close relationship with the uncertain geological parameters, such as the in situ stress, the joint configurations, and the joint mechanical properties. Therefore, the stability of the rock cavern should be studied with variable geological conditions. In this paper, the coupled hydro-mechanical model, which is under the framework of the discontinuous deformation analysis, is developed to study the underground cavern stability when considering the hydraulic pressure after excavation. Variable geological conditions are taken into account to study their impacts on the seepage rate and the cavern stability, including the in situ stress ratio, joint spacing, and joint dip angle. In addition, the two cases with static hydraulic pressure and without hydraulic pressure are also considered for the comparison. The numerical simulations demonstrate that the coupled approach can capture the cavern behavior better than the other two approaches without the coupling effects.

**Keywords** Discontinuous deformation analysis (DDA) · Coupled hydro-mechanical model · Geological conditions · Rock cavern stability

## 1 Introduction

The stability analysis of rock caverns is an important but complex issue due to underground water. During cavern excavation, the rock blocks may slide along the joint plane

or detach from the cavern roof because of the reduced shear and/or tensile strength of the rock joints. Especially, when the permeability around the cavern decreases significantly, a higher hydraulic gradient can be triggered around the cavern (Fernandez and Moon 2010a), which may lead to cavern instability. Therefore, the stability analysis for underground caverns considering the hydraulic condition should be studied.

Investigations for underground cavern stability have been carried out based on different geological conditions using numerical analysis. Yeung and Leong (1997) used the discontinuous deformation analysis (DDA) to study the tunnel stability under variable joint distributions, including variable joint orientation and spacing. Jia and Tang (2008) used the Rock Failure Process Analysis (RFPA) code (two-dimensional finite element code) to study the displacement development and the failure process for the underground tunnel. Different dip angles of the layered joints and variable lateral pressure coefficients are introduced for the stability analysis. Solak (2009) also studied different ground behaviors for the rock masses based on variable joint characteristics and in situ stresses using the Universal Distinct Element Code (UDEC). In the studies above, the structural stability has been well analyzed, but without the hydraulic effect. However, underground water normally exists in most of the cases. The hydraulic pressure should be considered when we investigate the stability during excavation. Fernandez and Moon (2010a, b) used the UDEC to study the excavation-induced hydraulic conductivity reduction around the tunnel. The formation of the damage zone around the tunnel was discussed based on the alteration of the fracture permeability in the vicinity of the tunnel after the excavation. In addition, the joint hydro-mechanical conditions are analyzed based on the pore pressure distribution and joint properties.

---

✉ Z. Y. Zhao  
czzhao@ntu.edu.sg

<sup>1</sup> School of Civil and Environmental Engineering, Nanyang Technological University, Singapore 639798, Singapore

<sup>2</sup> Land Transport Authority, Singapore 239711, Singapore

Besides the UDEC, the DDA approach under the discrete element method (DEM) framework is another alternative method to study the stability of underground excavation when underground water exists. To study the seepage rate and also the displacement development around the underground excavation comprehensively, a preliminary DDA-based coupled hydro-mechanical model is employed for the case study. Two underground rock caverns are modeled by considering variable hydro-geological conditions. The case studies include the change of the total inflow rate and the vertical displacements at the cavern roofs under different in situ stress ratios, the cavern stability under different joint spacing and the joint dip angles, and the stability analysis under two other methods for the hydraulic pressure modeling, where the underground water is expressed either with the static hydraulic pressure or is totally ignored. The results from these two methods will be compared with those obtained from the coupled hydro-mechanical model.

## 2 Methodology of the Coupled Hydro-Mechanical Model

### 2.1 Equations for Block Deformation and Movement

The DDA approach is used for modeling the mechanical behaviors of the discontinuous blocky systems. In DDA, the large displacements and deformations of the rock blocks can be considered by accumulating the small displacements and deformations from the previous time steps. Also, the rotation can be considered for the rock blocks (Shi 1988).

Each rock block in DDA has six degrees of freedom. The displacement  $(u, v)$  at any point  $(x, y)$  of the rock block can be represented by a complete first-order approximation function (Shi 1988; Jing 2003; Hatzor et al. 2004; Ning and Zhao 2013):

$$\begin{pmatrix} u \\ v \end{pmatrix} = \begin{pmatrix} 1 & 0 & -(y - y_0) & (x - x_0) & 0 & (y - y_0)/2 \\ 0 & 1 & (x - x_0) & 0 & (y - y_0) & (x - x_0)/2 \end{pmatrix} \begin{pmatrix} u_0 \\ v_0 \\ r_0 \\ \varepsilon_x \\ \varepsilon_y \\ \gamma_{xy} \end{pmatrix} \quad (1)$$

where  $(x, y)$  are the coordinates of any point within the rock block;  $(x_0, y_0)$  are the coordinates of a point within the rock block, which is usually taken at the block centroid;  $u_0, v_0$  are the rigid body translations at the point  $(x_0, y_0)$  along the  $x$ - and  $y$ -directions, respectively;  $r_0$  is the rigid body rotation angle in radians around the point  $(x_0, y_0)$ ;  $\varepsilon_x, \varepsilon_y, \gamma_{xy}$

are the normal and shear strains in the block. These six unknowns correspond to the general block deformation and movement.

In the DDA method, the block system can be formed through the contacts among the rock blocks and the constrained displacements of single blocks. Assuming that there are  $n$  blocks in the block system, then the global equation can be expressed by:

$$[K]\{d\} = \{F\} \quad (2)$$

where  $[K]$  is the material/contact matrix,  $\{d\}$  is the deformation sub-matrix, and  $\{F\}$  is the loading sub-matrix distributed to the six deformation variables.

### 2.2 Cubic Law for Fracture Flow

The cubic law can be used to describe the fluid flow within a single plated fracture. It was verified that the fluid pressure can be linearized section by section if the fractures are small. To simplify the coupled DDA hydro-mechanical model, the cubic law is employed to evaluate the hydraulic head distribution approximately, although a wide joint spacing is used to cut the rock blocks for all the case studies. Therefore, the hydraulic pressure is still linearized along the fractures. Moreover, the joint apertures are considered to be relatively small and only the steady flow is taken into account in this paper.

The mass conservation is guaranteed for each intersection point within the fracture network (Witherspoon et al. 1980; Jing et al. 2001), and the governing equation for the fracture fluid flow can be defined as:

$$\sum_{j=1}^n A_{ij} \frac{\rho g (b_{ij})^3}{12\mu} \frac{H_i - H_j}{L_{ij}} = 0 \quad (3)$$

where  $A_{ij}$  denotes the connection relationship between the intersection points  $i$  and  $j$  ( $i, j = 1, 2, \dots, n$ ). If  $i$  and  $j$  are the two end points of a fracture,  $A_{ij}$  is equal to 1; otherwise,  $A_{ij}$  is 0.  $\rho$  is the fluid density;  $g$  is the gravitational acceleration;  $b_{ij}$  is the equivalent hydraulic aperture for the fracture  $ij$ ;  $\mu$  is the fluid dynamic viscosity;  $H_i$  and  $H_j$  are the hydraulic heads at the intersections  $i$  and  $j$ , respectively;  $L_{ij}$  is the length of the fracture  $ij$ . From Eq. (3), the fracture transmissivity per unit length can be defined by:

$$T_f = \frac{\rho g (b_{ij})^3}{12\mu L} \quad (4)$$

where  $T_f$  is the fracture transmissivity per unit length.

From Eqs. (3) and (4), both the flow rate and the fracture transmissivity are sensitive to the aperture. The aperture, therefore, needs to be updated properly in each time step. The method proposed by Esaki et al. (1999) is adopted to update the aperture by:

$$b = b_0 + \Delta b_n \tag{5}$$

where  $b_0$  is the initial mechanical aperture and  $\Delta b_n$  is the normal closure of the fractures. When  $\Delta b_n > 0$ , it denotes that the fracture is open.

Equation (5) is easy to be implemented in DDA. In each time step, the normal distances on two end points of each block edge will be updated. The corresponding aperture, therefore, can be calculated for each end point. In general, the apertures at two end points are not the same and the fracture plate becomes non-parallel. Under this condition, an equivalent aperture is needed for the fluid flow analysis, which can be calculated by Jing et al.'s method (Jing et al. 2001).

Collecting all the equations from all the intersection points with the connection condition of the fracture network, the global equation of fluid flow can be expressed by (Jing et al. 2001; Chen et al. 2013):

$$[A][T_f]\{H\} = 0 \tag{6}$$

where  $[A]$  is the connection matrix described in Eq. (3);  $[T_f]$  is the fracture transmissivity matrix from Eq. (4);  $\{H\}$  is hydraulic head sub-matrix.

### 2.3 Hydro-Mechanical Coupling Process

Combining DDA in Eq. (2) and the fracture flow in Eq. (6), the coupled hydro-mechanical model can be set up as follows (Jing et al. 2001; Cammarata et al. 2007; Chen et al. 2013):

$$\begin{bmatrix} AT_f(b) & 0 \\ 0 & K \end{bmatrix} \begin{pmatrix} H \\ d(b) \end{pmatrix} = \begin{pmatrix} 0 \\ F \end{pmatrix} \tag{7}$$

where  $[A]$  is the connection matrix;  $[T_f(b)]$  is the fracture transmissivity matrix;  $\{H\}$  is the hydraulic head sub-matrix;  $[K]$  is the material/contact matrix;  $\{d(b)\}$  is the deformation sub-matrix;  $\{F\}$  is the loading sub-matrix.

The basic procedure for solving the coupled equation is briefly discussed. Firstly, the hydraulic head on each intersection point within the fracture network is calculated by Eq. (3). Subsequently, each hydraulic head is converted into the hydraulic pressure and applied onto the relevant DDA block. The solid mechanical analysis is carried out by DDA, after which the joint aperture can be adjusted based on the block deformation. The fracture transmissivity in Eq. (4) is updated and interpolated into the coupled DDA hydro-mechanical computation process for the next time step. The calculation does not stop until the last time step, shown in Fig. 1.

There are two assumptions for the numerical analysis in this paper. Firstly, as the blocky system is supposed to have small deformation or movement, the change of the fracture network is not taken into consideration. Second, all the

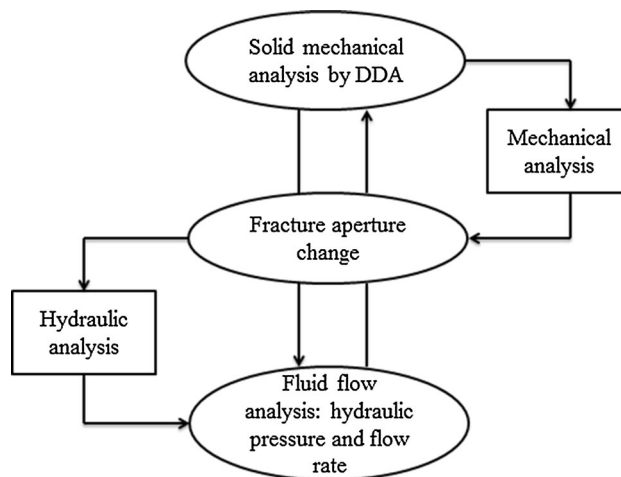


**Fig. 1** Framework for the coupled discontinuous deformation analysis (DDA) hydro-mechanical model (Rutqvist and Stephansson 2003)

physical parameters used for the validation cases remain constant during the numerical analysis. In fact, the current coupled DDA hydro-mechanical model has been verified through the inflow rate evaluation for the underground caverns (Chen et al. 2013). In this paper, we focus on the stability of underground caverns by taking the hydraulic pressure and variable geological conditions into consideration. Therefore, this paper is an extension to our previous work (Chen et al. 2013).

### 3 Underground Cavern Stability Analysis with Variable Geological Properties

To study the underground cavern stability after excavation, a rock cavern project is used for the case study. In this model, the whole DDA model dimensions are 200 m in width and 167 m in height. There are two horseshoe-shaped caverns (named cavern a and cavern b) located 119 m below the ground level. Each cavern is 20 m in width and 27.5 m in height, and the cavern roof is located at -119 mACD (“Admiralty Chart Datum”). The distance between the two caverns is 40 m, as shown in Fig. 2. Two joint sets frequently appearing along the excavation length have the orientations (strike/dip) 180°/80° and 90°/80°, respectively (Fig. 3). Four stiff rock blocks are created along the problem domain to generate the initial stress for each rock block (Figs. 2, 3). In addition, the rock blocks around the two excavation boundaries are all constrained by the fixed points initially. After the whole blocky system becomes steady under the initial stress, the fixed points are deleted. The purpose is to model a similar stress field for the rock blocks as soon as the caverns are excavated. There are four checked points above each cavern roof to check

**Fig. 2** Cross-section of the simulation model for the case study

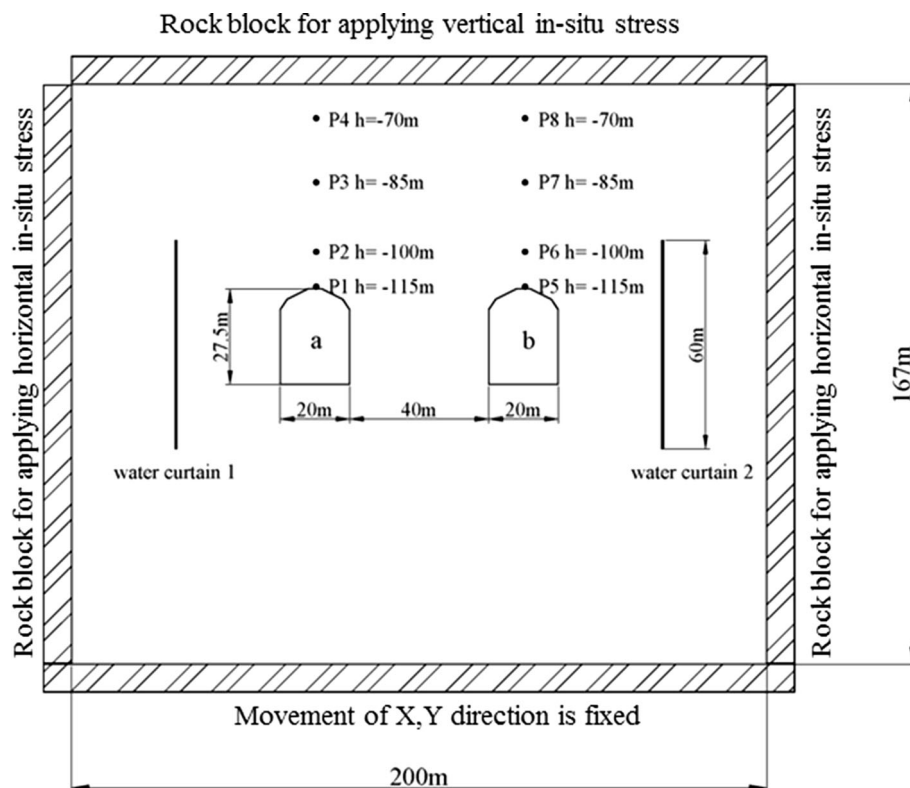
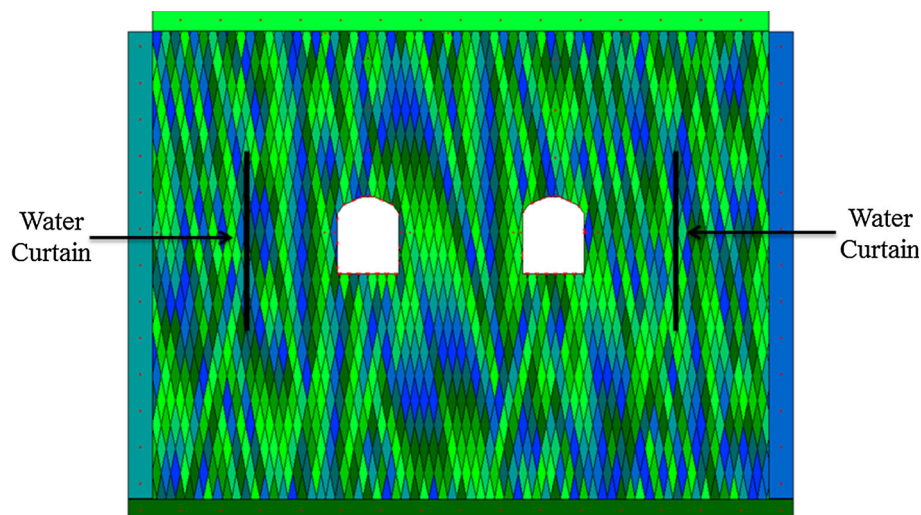


**Fig. 3** Simulation model in the DDA approach



the vertical displacements at four different depths:  $-115$ ,  $-100$ ,  $-85$ , and  $-70$  mACD.

The sea surface is located at  $0$  mACD and the sea bottom is at  $-15$  mACD. According to the hydraulic conductivity distribution in different stratum from the site investigation (Sun and Zhao 2010), the top surface of the simulation model is determined at  $-60$  mACD. A constant water head boundary with  $H = 0$  is applied to the top surface, which is equal to a water pressure generated by a  $60$ -m water column. For the other three boundaries of the

model, they are impermeable (Sun and Zhao 2010; Sun et al. 2011). In addition, the water curtains are put into operation to prevent the desaturation of the rock mass during the construction of the two caverns, which are modeled with two slim rock blocks in the model (Fig. 3). Along the water curtains, the hydraulic heads are  $H = 0$ . Moreover, the hydraulic pressure is equal to  $0$  Pa along the two excavation boundaries. The cross-section for the DDA model is shown in Fig. 3 and detailed DDA parameters for the simulation are shown in Table 1.

**Table 1** Detailed parameters used in the discontinuous deformation analysis (DDA) simulation

Block material parameters		Joint material parameters	
Block density (kg/m <sup>3</sup> )	2650	Joint set 1 (strike/dip)	180°/80°
Young's modulus (GPa)	40 (case1)	Joint set 2 (strike/dip)	90°/80°
	30 (case 2)	Spacing for joint set 1 (m)	3
Contact stiffness (GPa)	400 (case 1)	Spacing for joint set 2 (m)	3
	300 (case 2)	Friction angle	40°
Displacement ratio	1e-3	Cohesion (MPa)	1
Time interval (s)	2.5e-4	Tension strength (MPa)	0.5
Poisson's ratio	0.25	Initial aperture (m)	8e-5
		Residual aperture (m)	4e-5

### 3.1 Effect of In Situ Stress

The seepage can be influenced by the stress conditions. When the cavern is excavated, the stress is redistributed around the opening. Due to the redistributed stress, the fracture aperture is deformed and the fracture transmissivity is changed. Under this condition, the inflow into the cavern is affected, which, in turn, influences the stress redistribution (Ivars 2006). In addition, if the redistributed stress surpasses the strength of the surrounding rocks, the rocks can reach failure (Kinoshita et al. 1992). However, the main factors affecting the development of the redistributed stress are always from the strength, orientation, and distribution of the initial in situ stress (Gale and Blackwood 1987). Therefore, to study the in situ stress effect, five in situ stress conditions are applied for the numerical analysis to study the change in the total inflow rate of the two caverns and the vertical displacements above the two cavern roofs.

#### 3.1.1 Site Investigation for the In Situ Stress

The in situ stress regime is derived at the location of the underground cavern, which was tested close to the project zone using the hydraulic fracturing technique. In each hydraulic fracturing test, the fluid is injected into sealed off borehole intervals to induce and propagate hydraulic fractures in the rock mass. The stress regime in the rock mass can be determined from the pressure data during the hydraulic fracturing test (Zhao et al. 2005). The distribution of the maximum and minimum horizontal in situ stress was obtained from ten hydraulic fracturing tests in one vertical borehole at depths between 80 and 170 m below the sea bottom. And the vertical in situ stress was taken as the overburden pressure at the test location, i.e.:

$$\sigma_v = 0.70 + 0.0265(z - 27) \tag{8}$$

where  $\sigma_v$  is the vertical stress (MPa) and  $z$  is the depth below the sea bottom (m).

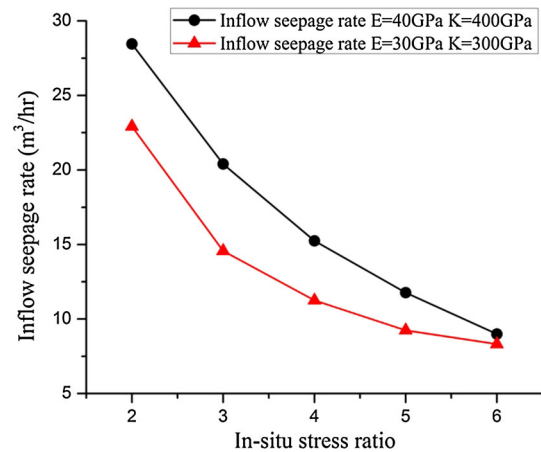


**Fig. 4** Total inflow rate of the two caverns under different in situ stress ratios

At a depth of 105 m below the sea bottom, the minimum ratio of the horizontal in situ stress to the vertical in situ stress is around 1.5, and the maximum ratio of the horizontal in situ stress to the vertical in situ stress is around 2.6. In addition, both the hydraulic fracturing test and laboratory experiments were carried out by Zhao and his colleagues in 2005 (Zhao et al. 2005) to obtain the in situ stress conditions for the underground granite in Singapore. From their observations, the in situ stress ratio is in the range of 2–6. Therefore, in situ stress ratios within the range 2–6 are applied for the simulation.

As the upper boundary of the model is at a depth of -60 mACD, the vertical in situ stress is around 1.2 MPa for all the case studies from Eq. (8). Corresponding to five different in situ stress ratios, the horizontal in situ stress is: 2.4, 3.6, 4.8, 6.0, and 7.2 MPa. The vertical and horizontal in situ stress will be applied on the boundaries of the numerical model (Fig. 2).

#### 3.1.2 Simulation Results on the In Situ Stress Effect

At the very beginning, the fractured rock mass at the excavated depth of 119–146 m with a Young's modulus for

**Table 2** The percentage seepage rate reduction for the in situ stress ratios of 3–6, compared with the seepage rate at the in situ stress ratio of 2

In situ stress ratio	Rock material 1 (40 GPa) (%)	Rock material 2 (30 GPa) (%)
3	28.32	36.43
4	46.45	50.91
5	58.64	59.68
6	68.41	63.74

the rock mass of 40 GPa is applied for the simulation. In Fig. 4, the inflow rate clearly decreases under a larger horizontal in situ stress. When the in situ stress ratio is 6, the inflow seepage rate is only 31.6 % of the value at the in situ stress ratio of 2. Subsequently, the fractured rock mass at the excavated depth of 146–168 m with the Young's modulus for the rock mass of 30 GPa is employed for the simulation again. The corresponding contact stiffness is changed to 300 GPa, which is ten times the Young's modulus. The inflow rate at an in situ stress ratio of 6 again remains only 36.3 % of the value at an in situ stress ratio of 2 (Fig. 4). The reduction of the inflow rate in both cases is around 65 %, as shown in Table 2. The results are in agreement with Indraratna and Wang (1996), who observed that the inflow water to the tunnel was reduced as the in situ stress ratio increases. In fact, the increased in situ stress ratio can make the effective normal stress around the excavation zone increase at the same time. As the fracture deformation depends on the effective stress strongly, the fracture aperture decreases dramatically by the increased effective stress (Fernandez and Moon 2010b). The inflow rate is, therefore, clearly reduced.

Figure 5 indicates that, when the hydraulic pressure is considered, the vertical displacements above the two cavern roofs decrease as a result of the increased in situ stress ratio, as the confining stress among the rock blocks is increased by the higher lateral stress. In particular, the higher lateral stress can be beneficial to the cavern roof stability to make the failure less significant (Gale and Blackwood 1987). The same trend can be found in Fig. 6. Overall, the vertical displacement development above the two cavern roofs follows the same rule as in the case without the hydraulic pressure (Jia and Tang 2008).

### 3.2 Effect of Joint Properties

Variable joint properties play important roles for the stability of underground rock caverns. Different failure modes can be found for the caverns when different joint properties are considered. In 2004, Solak and Schubert (2004) studied the stability of a circular tunnel and discussed the displacement change with different joint properties, including

the joint spacing, joint residual friction angle, and the block shape. Based on variable block shapes and joint spacing, they classified three failure modes for the rock blocks (Fig. 7). In Mode A, the rock blocks become steady soon after the cavern excavation. For the same block shape, the displacement increases as the block size decreases. For Mode B, a failure wedge occurs easily around the excavated boundary, which has a strong relationship with the block shape, block size, and the joint strength. And in Mode C, the shear failure can be found tangential to the tunnel. Also, the displacement can be reduced by decreasing the block apex angle.

As the underground water was not included in the stability analysis by Solak and Schubert (2004), the cavern responses are not known under the presence of hydraulic pressure. Thus, using Solak and Schubert's observations and classifications, the stability analysis is carried out by taking the underground water and variable joint properties into account at the same time. The purpose is to find out whether the displacement of the rock blocks above the cavern roofs and the cavern stability follow the same rules.

Different joint properties are considered for the case studies in the following, including the joint spacing and the joint dip angles, which are obtained through the geological mapping from the project zone. In particular, along the excavated length, there are three joint sets at a certain location. Two of them are selected to create the rock blocks for the simulation model. Three combinations of the joint dip angles appear frequently, which are listed in Table 3. In addition, at the excavated length of 215 m, there is one more combination of dip/dip angles of 50°/85°. Among the four cases in Table 3, Case7090, Case8080, and Case7080 belong to Mode A, while Case5085 belongs to Mode B (Fig. 7). As the maximum in situ stress ratio from the site data is around 2–3, the in situ stress ratio is fixed at 3 for all the following case studies.

#### 3.2.1 Effect of Joint Spacing

Case8080 and Case7090 are selected to study the effect of joint spacing. Along the excavated length, the spacing of the joint sets is medium (20–60 cm) or very wide (larger than 200 cm). In order to cut down the total number of rock blocks in the DDA model, wide joint spacings are chosen for both joint sets, including 4, 3, and 2 m, respectively.

Without the hydraulic pressure, the vertical displacements above the two cavern roofs follow the rule in Mode A, which increase with decreased rock block size (Figs. 8, 9). In particular, each rock block is constrained by the surrounding rock blocks in DDA. It is found that the block sizes and shapes are slightly different for the rock blocks surrounding the two caverns; therefore, the constraints between these rock blocks are different. That is why the

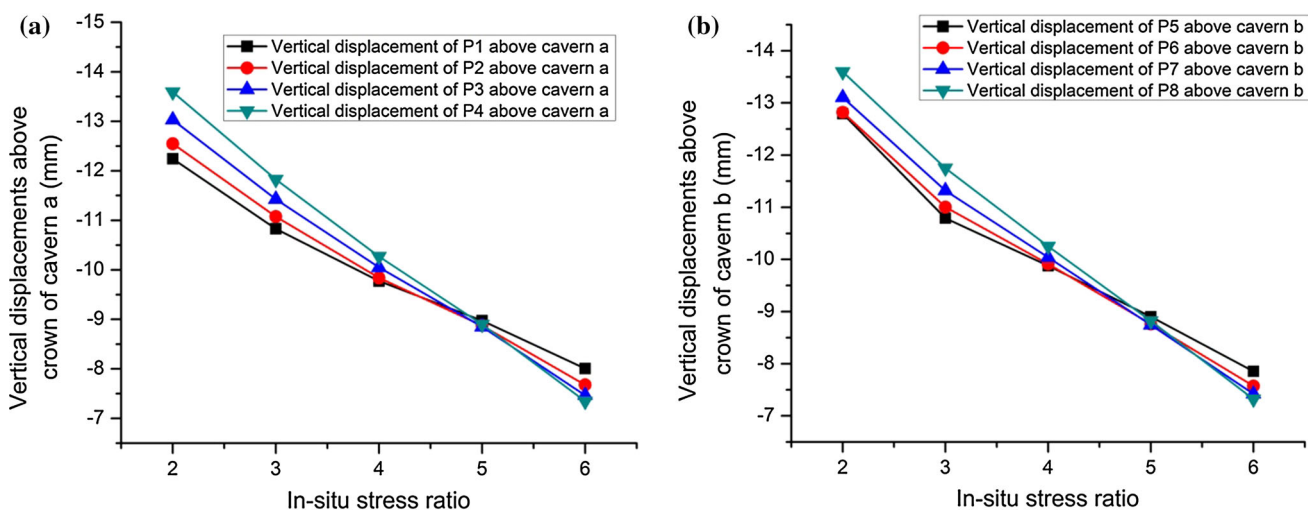


Fig. 5 Vertical displacements ( $E = 40$  GPa): a P1–P4 above cavern a; b P5–P8 above cavern b

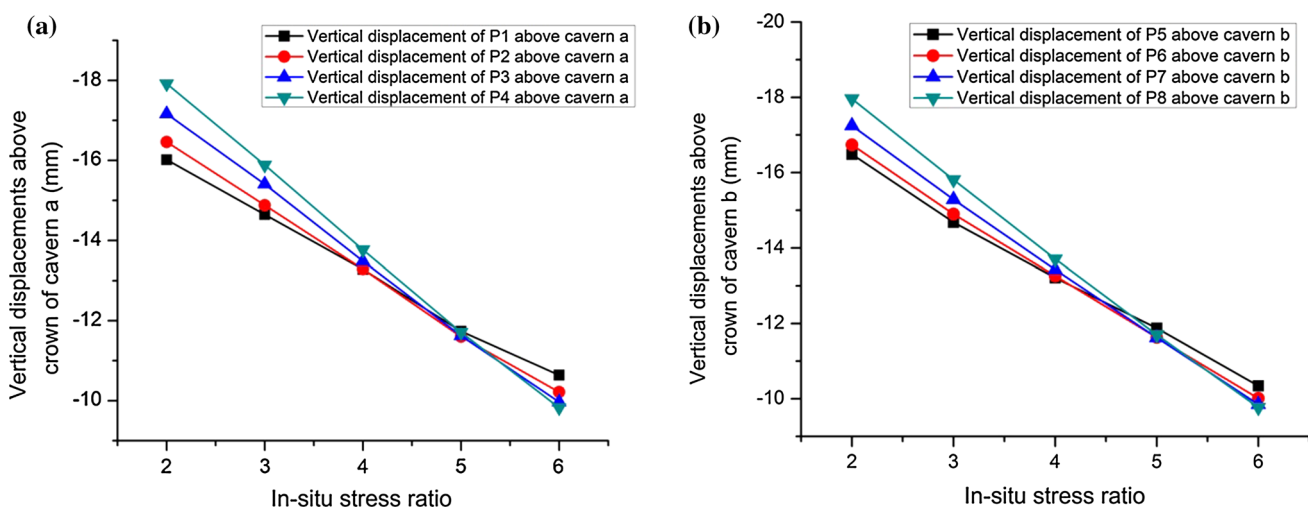
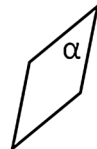


Fig. 6 Vertical displacements ( $E = 30$  GPa): a P1–P4 above cavern a; b P5–P8 above cavern b

Fig. 7 Classification of the failure modes for rock blocks with different sizes and joint strengths (Solak and Schubert 2004)

 $\alpha = 10^\circ - 80^\circ$	Apex Angle for Rock Block ( $\alpha$ )															
	10°		20°		30°		40°		50°		60°		70°		80°	
Joint strength	H	L	H	L	H	L	H	L	H	L	H	L	H	L	H	L
JS=2m	A	A	A	A	B	B	C	C	C	C	C	C	C	C	C	C
JS=1m	A	A	A	A	B	B	B	B	B	B	C	C	C	C	C	C
JS=0.5m	A	A	A	A	B	B	B	B	B	B	B	C	C	C	C	C

(H: high joint strength; L: low joint strength; JS: joint spacing; A: Mode A; B: Mode B; C: Mode C)

vertical displacements for P1 and P2 above cavern a are distinctly different from P5 and P6 above cavern b (Figs. 8, 9).

When the hydraulic pressure is applied for Case8080, the largest vertical displacements for the eight checked points above the cavern roofs occur at 2 m joint spacing (Fig. 10). As can be seen, most of the checked points follow the same rule for the rock block in Mode A (Fig. 7), in that the displacement increases as the block size decreases.

In Case7090, P1 above cavern a has the largest vertical displacement at 4 m joint spacing when compared with those obtained from 2 and 3 m joint spacings (Fig. 11a). This is due to the rock block near the excavation boundary, in which the checked point P1 is located. At 2 or 3 m joint spacings, this rock block has a pentagonal shape for both cases. For 4 m joint spacing, the rock block has a triangular shape. Supposing that only the block weight and the applied hydraulic pressure are considered for three rock blocks, then based on the force equilibrium for the pentagonal rock block, parts of the hydraulic pressure components in the  $x$ - and  $y$ -directions on the block boundaries are canceled out (Fig. 12a). But for the triangular rock

block, only the horizontal hydraulic pressure components are largely canceled out, as the vertical ones are accumulated for the rock block (Fig. 12b). Therefore, the triangular-shaped rock block will bear more vertical pressure than the pentagonal one, in that the vertical displacement is possibly larger.

Except for P1, the largest vertical displacements for P2–P4 above cavern a in Case7090 can be obtained at 2 m joint spacing, and the displacements at 3 m joint spacing are quite close to the values when the joint spacing is 4 m (Fig. 11a). For cavern b, the largest vertical displacements for P5–P8 occur at 2 m joint spacing (Fig. 11b).

Based on Case8080 and Case7090, the displacement developments above the two cavern roofs basically follow the rule in Mode A (Fig. 7), in that the vertical displacement increases as the block size decreases. However, when considering the hydraulic pressure, the vertical displacement above the cavern roofs appears locally different from those without the hydraulic pressure. It indicates that the displacement development for the rock block is not only related to the block size, but also the block shape created by the discontinuities.

### 3.2.2 Effect of Joint Angle

Figures 13 and 14 are Case7090 and Case8080, respectively. At 3 m joint spacing, the caverns in those two cases become stable soon after the excavation. Although there are some local failures on the sidewalls for cavern a in Case8080, the results are quite consistent with the description for the rock block behaviors around the excavated opening for Mode A. In particular, the block sizes in these two cases are nearly the same; however, most of the vertical displacements from Case8080 are slightly larger than

**Table 3** The strike/dip angles for the combinations of joint sets along the excavated length

Combinations of two joint sets along the excavated length (strike/dip)	Combinations of the joint dip angles for the simulations (strike/dip)
90°/70°, 180°/80°	70°/80° (Case7080)
90°/70°, 180°/90°	70°/90° (Case7090)
90°/80°, 180°/80°	80°/80° (Case8080)
140°/50°, 180°/85°	50°/85° (Case5085)

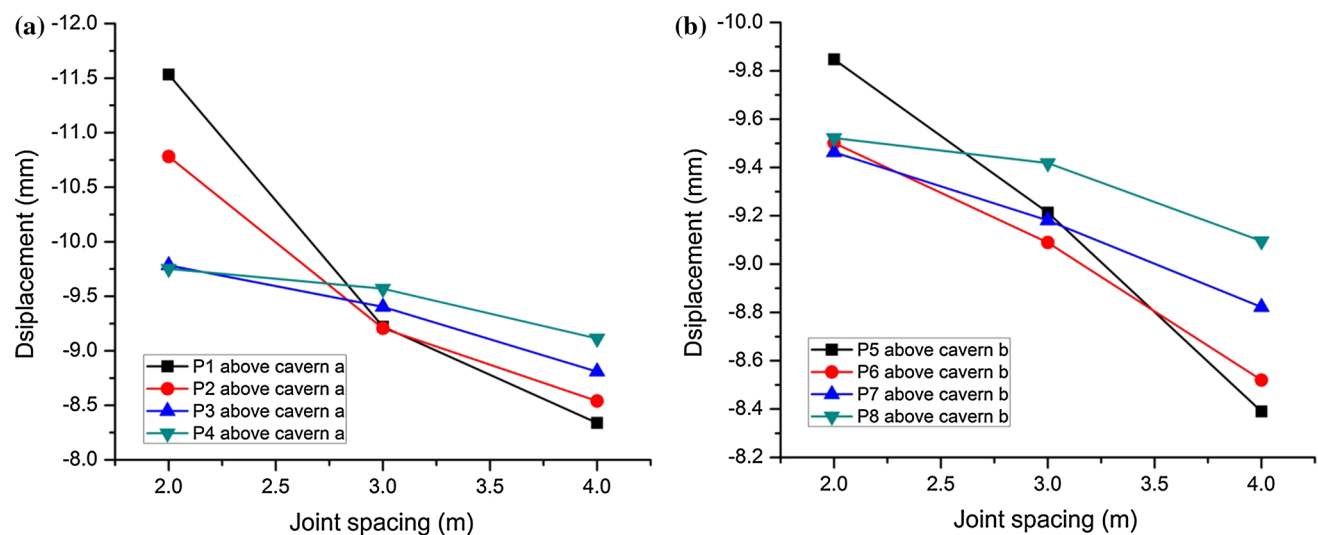


**Fig. 8** Vertical displacements without the hydraulic pressure for Case8080: **a** P1–P4 above cavern a; **b** P5–P8 above cavern b



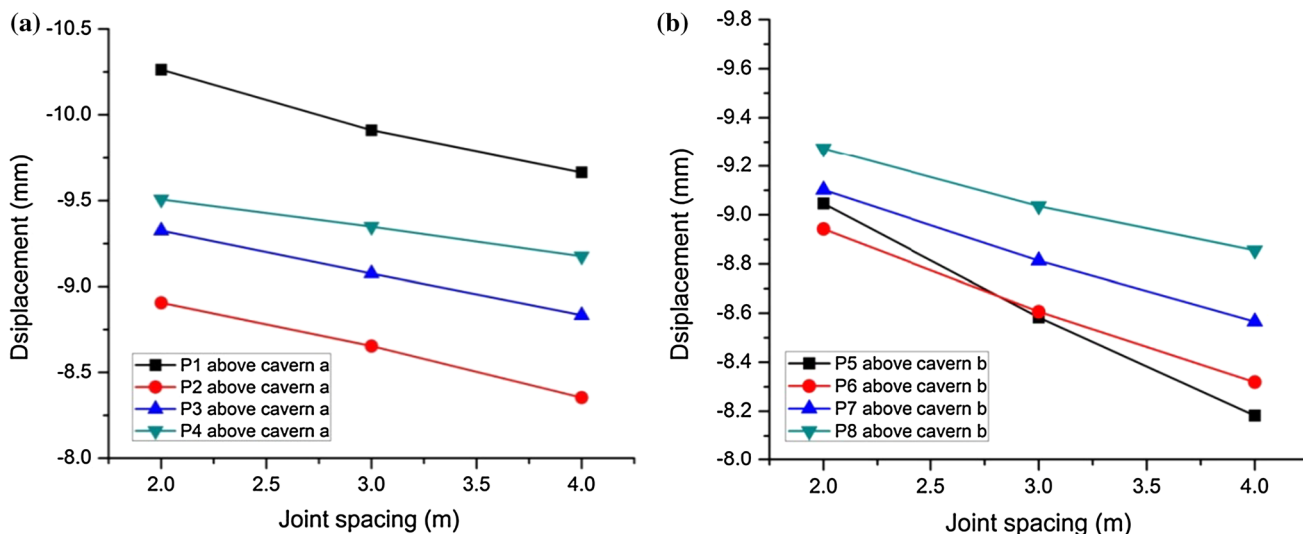


Fig. 9 Vertical displacements without the hydraulic pressure for Case7090: a P1–P4 above cavern a; b P5–P8 above cavern b

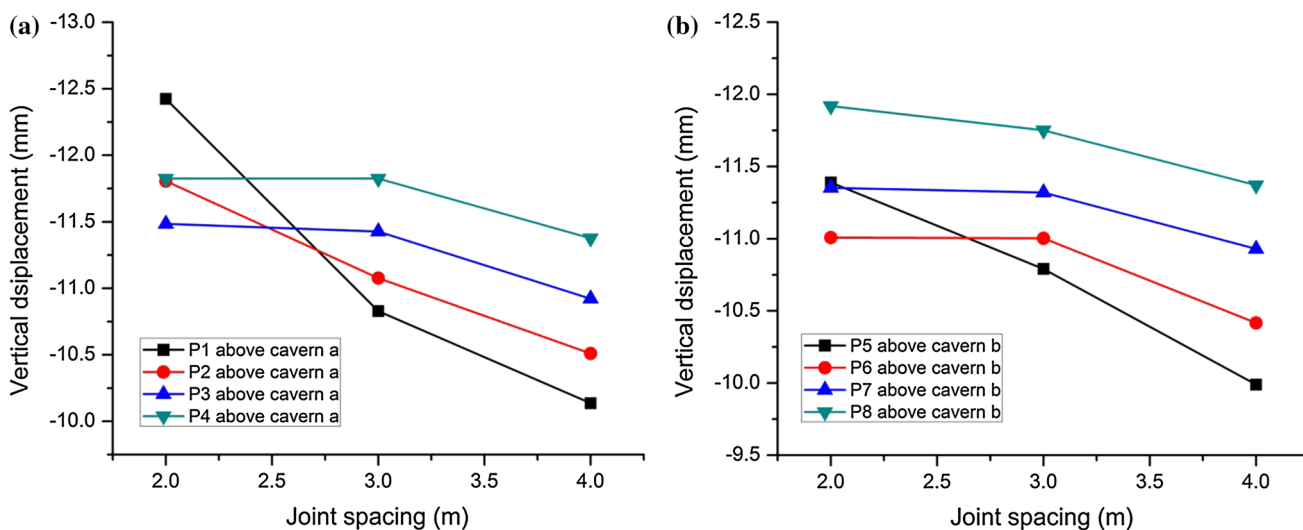


Fig. 10 Vertical displacements with the hydraulic pressure for Case8080: a P1–P4 above cavern a; b P5–P8 above cavern b

those from Case7090 (Table 4). The block shape is assumed to be the factor affecting the displacement development of the rock blocks under the hydraulic pressure, which needs further discussion.

In Case7080 (Fig. 15), a failure wedge is formed above cavern b, leading to local collapse. One of the reasons for this is the existence of the hydraulic pressure. Both caverns are stable without considering the hydraulic pressure. The vertical displacements are around 9.0 mm for P1 above cavern a and 9.4 mm for P5 above cavern b. However, when the hydraulic pressure is applied, some local shear failure can, therefore, be found on the sidewalls for both caverns (Fig. 15a); this is due to the reduced shear strength of the rock joint as a result of the decreased contact effective stress based on the Mohr–Coulomb criteria (Jing

et al. 2001; Chen et al. 2007). Moreover, as the joint can be opened due to the tensile failure or shear failure, the rock blocks become loose and can be detached from the adjacent blocks. If the joint opening propagates gradually, a failure wedge can be formed and drops down, which affects the cavern stability (Fig. 15b). The second reason is assumed to come from the block shape, which will be discussed next.

The rock blocks in Case5085 belong to Mode B (Fig. 7). Without the hydraulic pressure, the failure on the sidewalls is not so obvious, but cavern b locally collapses (Fig. 16). It was proposed that, if one of the joint angles is between 40° and 60°, a large deformation could be induced to result in a cavern instability (Zhu et al. 2004). After adding the hydraulic pressure, obvious shear failure can be seen on the

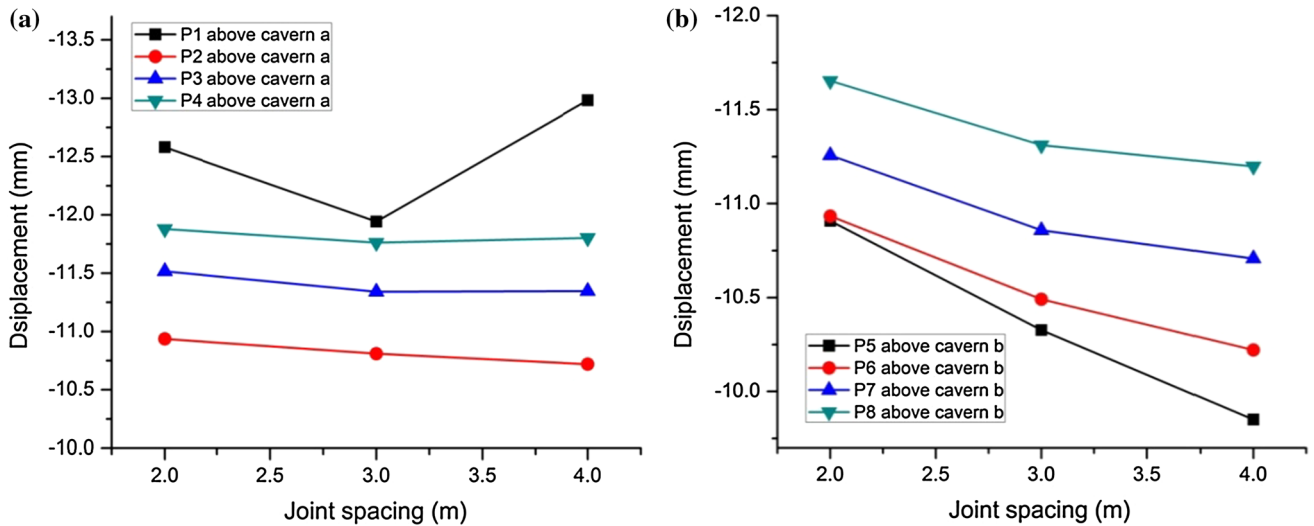


Fig. 11 Vertical displacements with the hydraulic pressure for Case7090: a P1–P4 above cavern a; b P5–P8 above cavern b

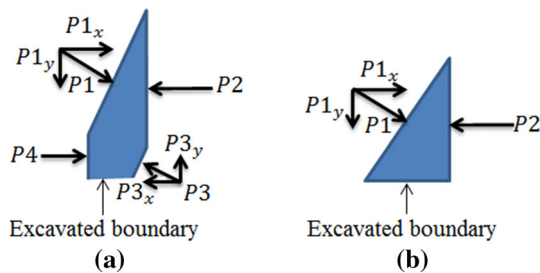


Fig. 12 External hydraulic loading for the rock block located at the excavated boundary in Case7090, with: a pentagonal shape for 2 and 3 m joint spacings and b triangular shape for 4 m joint spacing

sidewalls for both caverns (Fig. 17), which is caused by the excessive rock block sliding along the jointed plane (Solak 2009). Moreover, cavern b also collapses by the failure wedge (Fig. 17), and the failure wedge in Fig. 17b is larger than that in Fig. 16b. It is believed that the failure can be triggered even more easily and seriously under the hydraulic pressure. Overall, the response of the rock blocks in Case5085 approximately follows the described failure mode in Mode B (Fig. 7).

Comparing the above four cases, the change in the cavern stability is assumed to have a strong relationship with the block shape. From the block theory proposed by Goodman and Shi (1985), the asymmetric triangular roof prism is one of the potential unstable block shapes above the excavation (Chen et al. 1997). Therefore, in the following, a triangular roof prism above the excavated boundary is designed to approximate the safety factors for the four cases without the hydraulic pressure.

Following the relaxation analysis proposed by Brady and Brown (2004), the safety factor of the asymmetric triangular prism is given by:

$$SF = \frac{P}{W} \tag{9}$$

where  $P$  is the resistance in stopping the triangular prism from falling, which is related to the horizontal stress-induced frictional force (Chen et al. 1997);  $W$  is the prism weight.

$$P = H_0(P_1 + P_2) \tag{10}$$

in which:

$$P_1 = \frac{(k_s \cos^2 \alpha_1 + k_n \sin^2 \alpha_1) \sin(\phi - \alpha_1)}{k_n \sin \alpha_1 \sin \phi + k_s \cos \alpha_1 \cos \phi} \tag{11}$$

$$P_2 = \frac{(k_s \cos^2 \alpha_2 + k_n \sin^2 \alpha_2) \sin(\phi - \alpha_2)}{k_n \sin \alpha_2 \sin \phi + k_s \cos \alpha_2 \cos \phi} \tag{12}$$

$$W = \frac{\gamma h^2}{2} [\tan \alpha_1 + \tan \alpha_2] \tag{13}$$

where  $H_0$  is the internal horizontal force (Fig. 18) (Brady and Brown 2004);  $k_n$  and  $k_s$  are the joint normal contact stiffness and shear contact stiffness, respectively. In DDA,  $k_n$  is set to be 2.5 times  $k_s$  (Ning et al. 2012);  $\alpha_1$  and  $\alpha_2$  are the prism angles (Fig. 18);  $\phi$  is the joint friction angle;  $\gamma$  is the unit weight of the prism;  $h$  is the prism height; and in Fig. 18,  $N_0$  and  $S_0$  are the initial surface forces related to  $H_0$ .

Combining Eqs. (9)–(13), the safety factor is given by:

$$SF_d = \frac{2H_0}{\gamma h^2} \frac{P_1 + P_2}{(\tan \alpha_1 + \tan \alpha_2)} = m \frac{P_1 + P_2}{(\tan \alpha_1 + \tan \alpha_2)} \tag{14}$$

where  $SF_d$  is the safety factor for the roof prism without the hydraulic pressure.

Without the hydraulic pressure, the safety factor of the prism is related to the block apex angle based on Eq. (14).

**Fig. 13** Simulation result for the cavern stability in Case7090, with: **a** the whole domain and **b** zoomed area around the two caverns

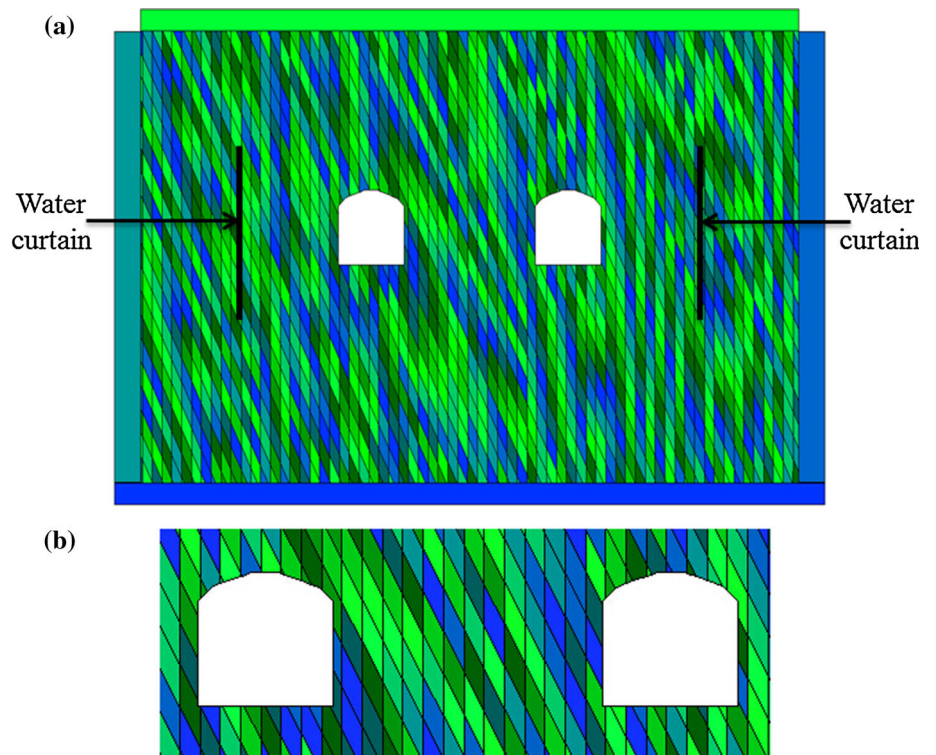


**Fig. 14** Simulation result for the cavern stability in Case8080, with: **a** the whole domain and **b** zoomed area around the two caverns

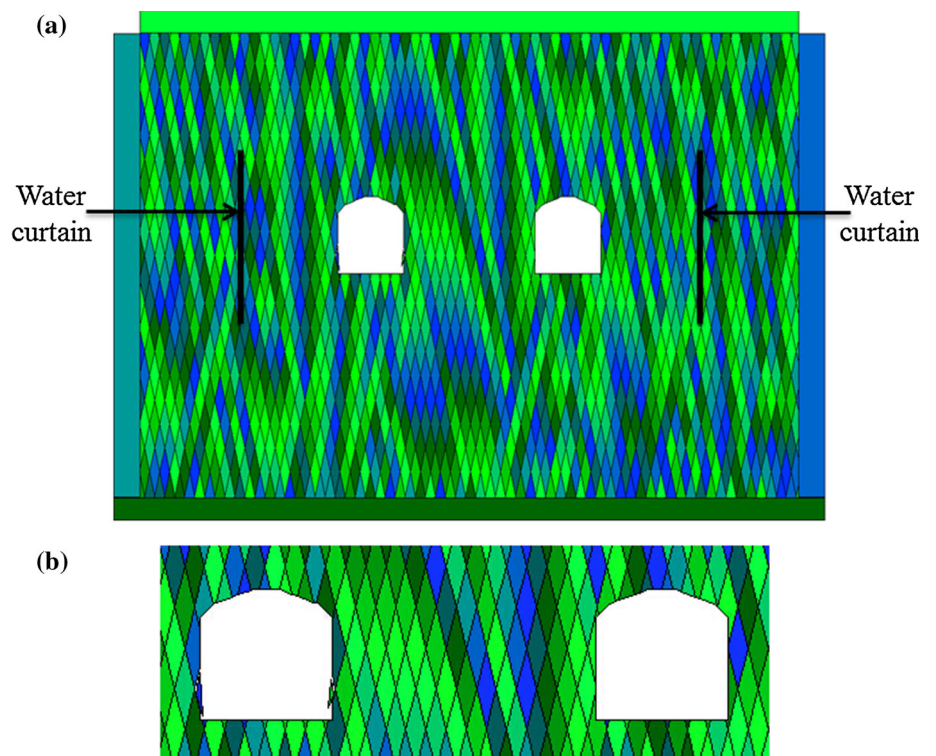


**Table 4** Vertical displacements under the two joint sets

Case	P1 (cm)	P2 (cm)	P3 (cm)	P4 (cm)	P5 (cm)	P6 (cm)	P7 (cm)	P8 (cm)
Case7090	-1.194	-1.081	-1.134	-1.176	-1.033	-1.049	-1.086	-1.131
Case8080	-1.083	-1.108	-1.143	-1.182	-1.079	-1.100	-1.132	-1.175

**Fig. 15** Simulation result for the cavern stability in Case7080, with: **a** failure on the two caverns and **b** failure wedge on cavern b

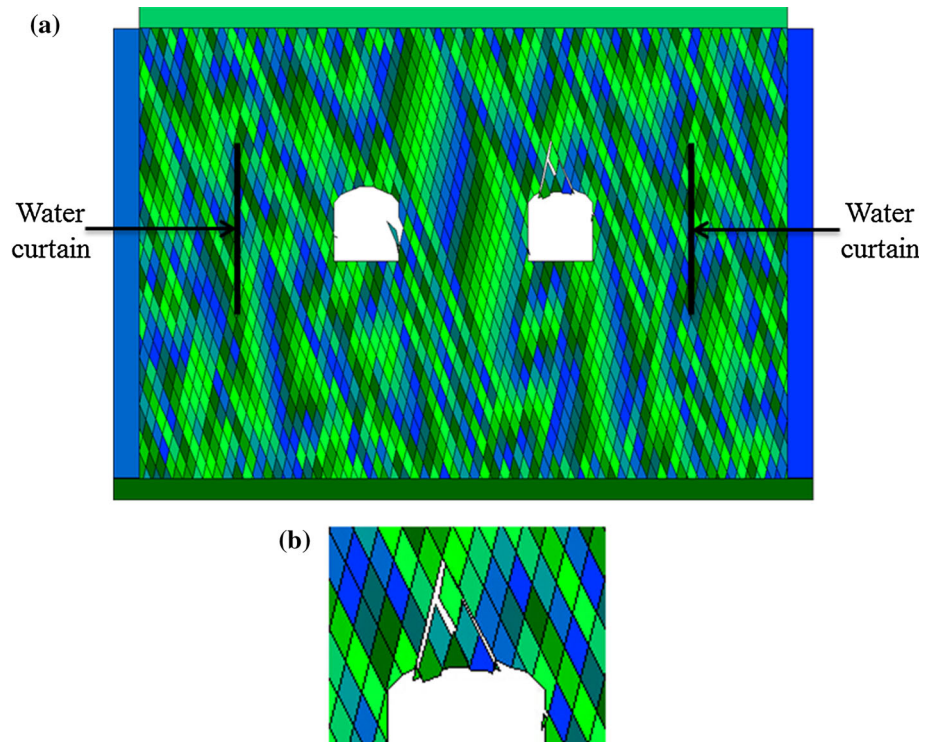


**Fig. 16** Simulation result for the cavern stability in Case5085 without the hydraulic pressure, with: **a** the whole domain and **b** failure wedge on cavern b

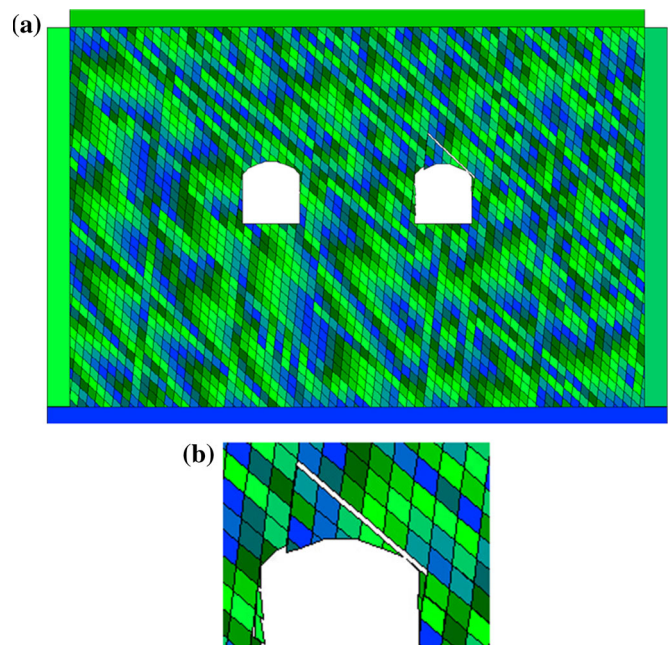


**Fig. 17** Simulation result for the cavern stability in Case5085 with the hydraulic pressure, with: **a** the whole domain and **b** zoomed area around the two caverns

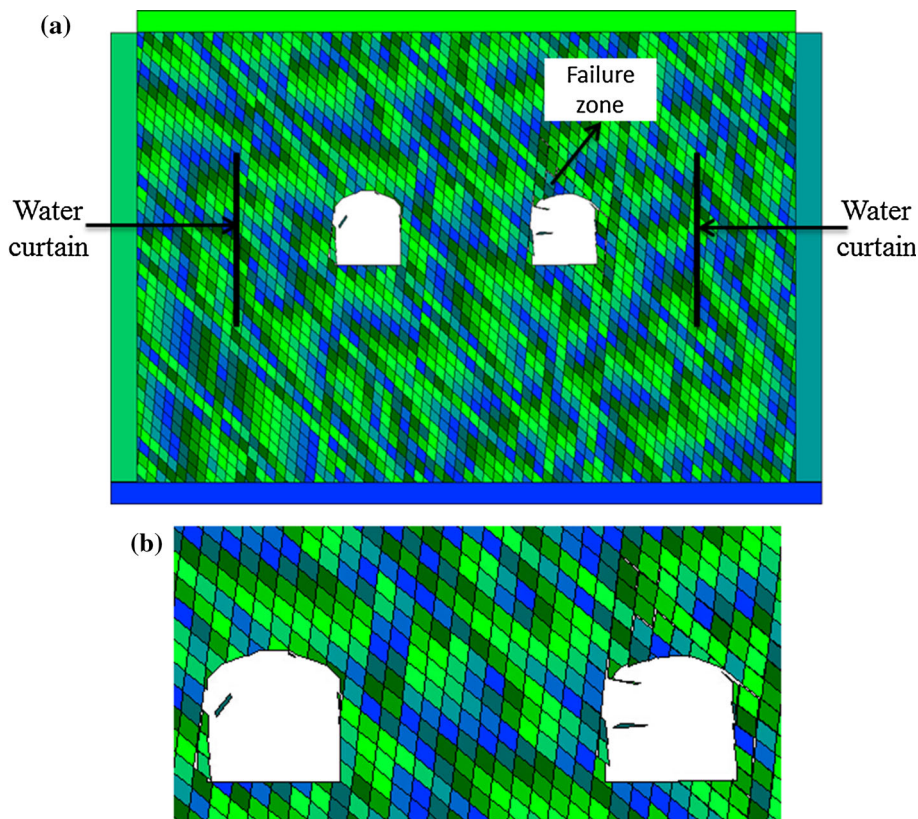
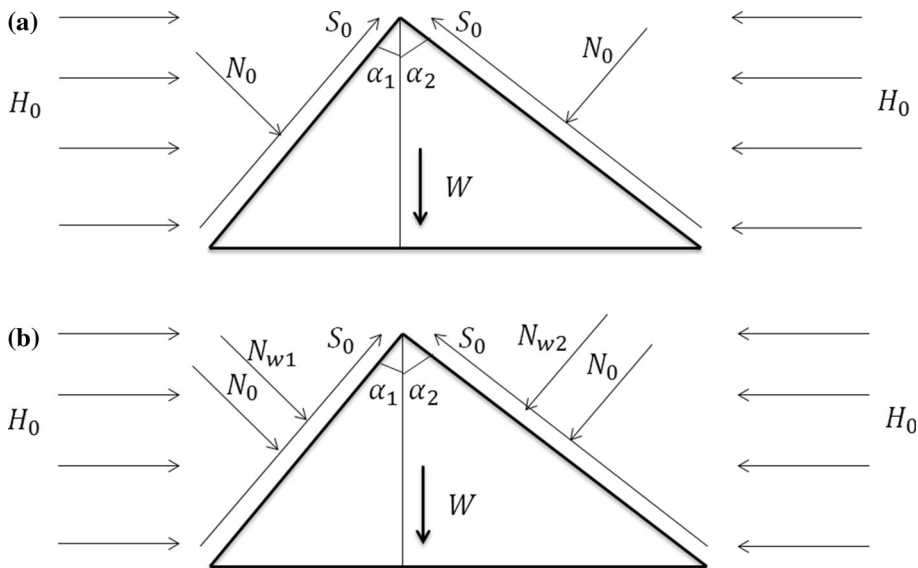


**Fig. 18** Asymmetrical triangular roof prism (Chen et al. 1997; Brady and Brown 2004): **a** without the hydraulic force and **b** with the hydraulic force



In order to simplify the calculation and better indicate the influence of the block shape,  $H_0$  and  $h$  are considered as constants for the four cases initially. Thus, a constant parameter  $m$  is employed to take the place of the  $\frac{2H_0}{\gamma h^2}$  in Eq. (14). The safety factors for Case7090, Case8080, Case7080, and Case5085 are 3.175  $m$ , 2.868  $m$ , 1.522  $m$ , and 0.693  $m$ , respectively, which gives Case5085 the

largest likelihood of cavern failure without the hydraulic pressure, which is consistent with the simulation result (Fig. 16).

Applying the hydraulic effect on the prism (Fig. 18b), the safety factor can be derived approximately following the relaxation analysis by Brady and Brown (2004), and is given as follows:

$$\begin{aligned}
SF_w &= \frac{H_0(P_1 + P_2) - \frac{k_s N_{w1} \cos \alpha_1 \sin(\phi - \alpha_1)}{k_n \sin \alpha_1 \sin \phi + k_s \cos \alpha_1 \cos \phi} - \frac{k_s N_{w2} \cos \alpha_2 \sin(\phi - \alpha_2)}{k_n \sin \alpha_2 \sin \phi + k_s \cos \alpha_2 \cos \phi}}{\frac{\gamma h^2}{2} (\tan \alpha_1 + \tan \alpha_2)} \\
&= SF_d - \frac{\frac{k_s N_{w1} \cos \alpha_1 \sin(\phi - \alpha_1)}{k_n \sin \alpha_1 \sin \phi + k_s \cos \alpha_1 \cos \phi} + \frac{k_s N_{w2} \cos \alpha_2 \sin(\phi - \alpha_2)}{k_n \sin \alpha_2 \sin \phi + k_s \cos \alpha_2 \cos \phi}}{\frac{\gamma h^2}{2} (\tan \alpha_1 + \tan \alpha_2)}
\end{aligned} \quad (15)$$

where  $SF_w$  is the safety factor for the roof prism with consideration of the hydraulic influence;  $P_1$  and  $P_2$  are from Eqs. (11) and (12);  $N_{w1}$  and  $N_{w2}$  are the hydraulic forces on the prism (Fig. 18b).

Equation (15) shows that the safety factor  $SF_w$  is clearly decreased by the hydraulic forces on the prism, as the contact effective stress on the jointed plane is reduced by the hydraulic pressure. Also, it proves that the safety factor for the roof prism is still related to the block apex angle under the hydraulic influence.

Besides the safety factor, the unsaturated zone is also found to influence the excavation stability. Initially, all the fractures are supposed to be saturated for the modeling; however, not all the fractures are filled with water from the site investigation. An unsaturated zone located above the roof of cavern b has been found in both Case7080 and Case5085 from the simulation results. Particularly, the location and shape of the unsaturated zones are quite similar to those of the failure wedges. Inside the unsaturated zone, the fracture aperture is too small to conduct fluid flow. The fluid can only flow through the fractures surrounding the unsaturated zone. However, most of these permeable fractures are also compressed tightly by the adjacent rock blocks, so the apertures are small. Under this condition, the hydraulic permeability around the unsaturated zone is much smaller than the other zones in the simulation domain. As a result, high hydraulic pressure can be generated and distributed around the unsaturated zone, which is similar to the grouting effect. If the hydraulic pressure surpasses the strength of the fractures surrounding the unsaturated zone, a failure wedge can be formed around the unsaturated zone. Besides Case7080 and Case5085, only small unsaturated areas can be found on the sidewalls in Case8080. After two small rock blocks drop down from the sidewalls, both caverns become stable in Case8080. For Case7090, there is no unsaturated zone. Therefore, it is believed that the formation of the unsaturated zone is also related to the block shape.

### 3.3 Comparison of Different Hydraulic Pressure Modeling

The underground water can be expressed with variable forms in the numerical analysis. The simulation results can be quite different when using different methods to take into account the underground water. In this comparison study,

two more methods are applied to study the vertical displacements above the cavern roofs when the in situ stress ratio changes from 2 to 6. Method one uses the static hydraulic pressure, while the underground water is neglected for method two. Two joint sets with dip/dip angles of  $80^\circ/80^\circ$  are applied for the simulation model, and the joint spacing is fixed at 3 m for each joint set. The vertical displacements of eight checked points obtained from these two methods will be compared with those from the coupled DDA hydro-mechanical model.

#### 3.3.1 Static Hydraulic Pressure

When the underground water is applied by the static hydraulic pressure, the hydraulic pressure on each intersection point within the fracture network can be calculated based on the hydraulic head and the elevation head of this point. With the hydraulic pressure on two nodal points of a fracture, the static hydraulic pressure can be applied along the fracture length and transferred to the mechanical analysis in DDA.

The blocks on the cavern roofs are stable when the static hydraulic pressure is applied under five in situ stress ratios (Fig. 19). However, serious failures still occur on the sidewalls and the bottom surface for both caverns under the static hydraulic pressure. Especially for the rock blocks on the bottom surface, they can heave and detach from the adjacent blocks quite soon after the static hydraulic pressure is applied. In practice, this failure can occur as soon as the cavern is excavated. When the cavern is excavated, the hydraulic pressure along the excavated boundary drops to zero in a short time. But the hydraulic pressure in the cavern vicinity remains at a high value at the very beginning, as it needs time to dissipate and adjust to the new surrounding hydraulic conditions. If the hydraulic pressure dissipates slowly, the rock blocks have to bear the high hydraulic pressure for a longer time. Under this condition, the rock blocks around the excavated boundary may fail easily if there is no supporting facility. Zhao and Gao (2009) indicated that, after the excavation, the largest seepage always occurs on the sidewalls and the bottom surface of the cavern under the high hydraulic pressure in these zones. Also, the stress redistribution occurs easily on the right and left corners of the bottom surface for the high compressive stress. These two factors can actually bring the cavern to disaster. That is why dramatic failure can be seen on the sidewalls and bottom surfaces of the caverns from the simulations.

In practice, the hydraulic pressure around the excavation zone dissipates gradually after the excavation, such that the displacement development of the rock blocks will slow down. If the hydraulic pressure dissipation is totally neglected for the numerical model, the hydraulic pressure always remains at a high value around the excavated

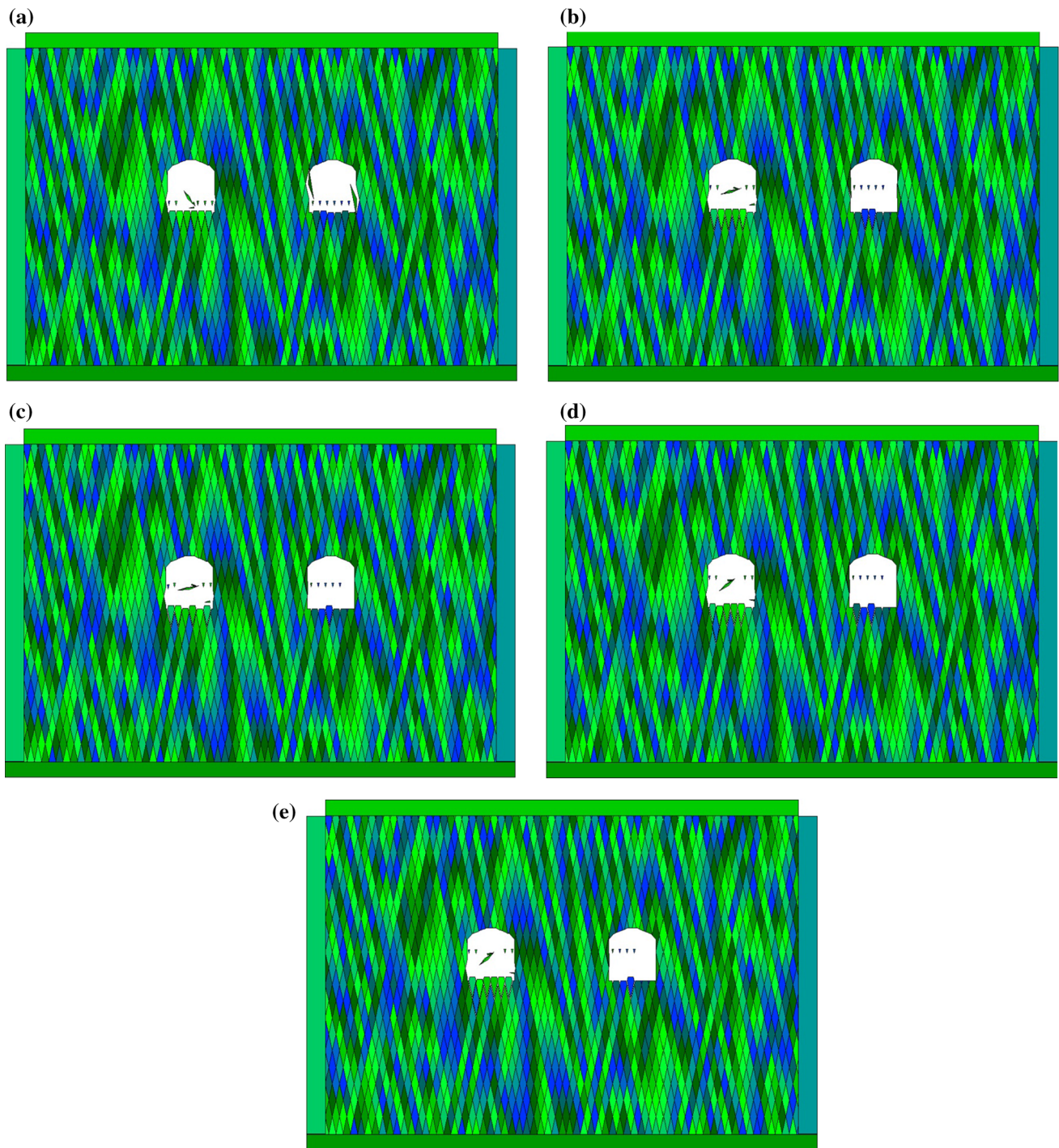


**Fig. 19** Stability analysis using the static hydraulic pressure model, with in situ stress ratios of: **a** 2, **b** 3, **c** 4, **d** 5, and **e** 6

boundary, such that excessive deformation occurs on the rock blocks. Therefore, the stability of the cavern is underestimated.

### 3.3.2 Neglecting Hydraulic Pressure

Sometimes, the underground water is neglected in the numerical analysis. The deformation above the cavern roofs

is, therefore, smaller than that when the hydraulic pressure is taken into account. In the excavation vicinity, when the in situ stress ratio is equal to 2, the displacements for P1 and P5 are 14.4 and 19.3 % smaller, respectively, than those from the coupled hydro-mechanical model. And for the zones away from the two caverns (P2–P4, P6–P8), the displacements are around 15–19 % smaller than the corresponding values when considering the hydraulic

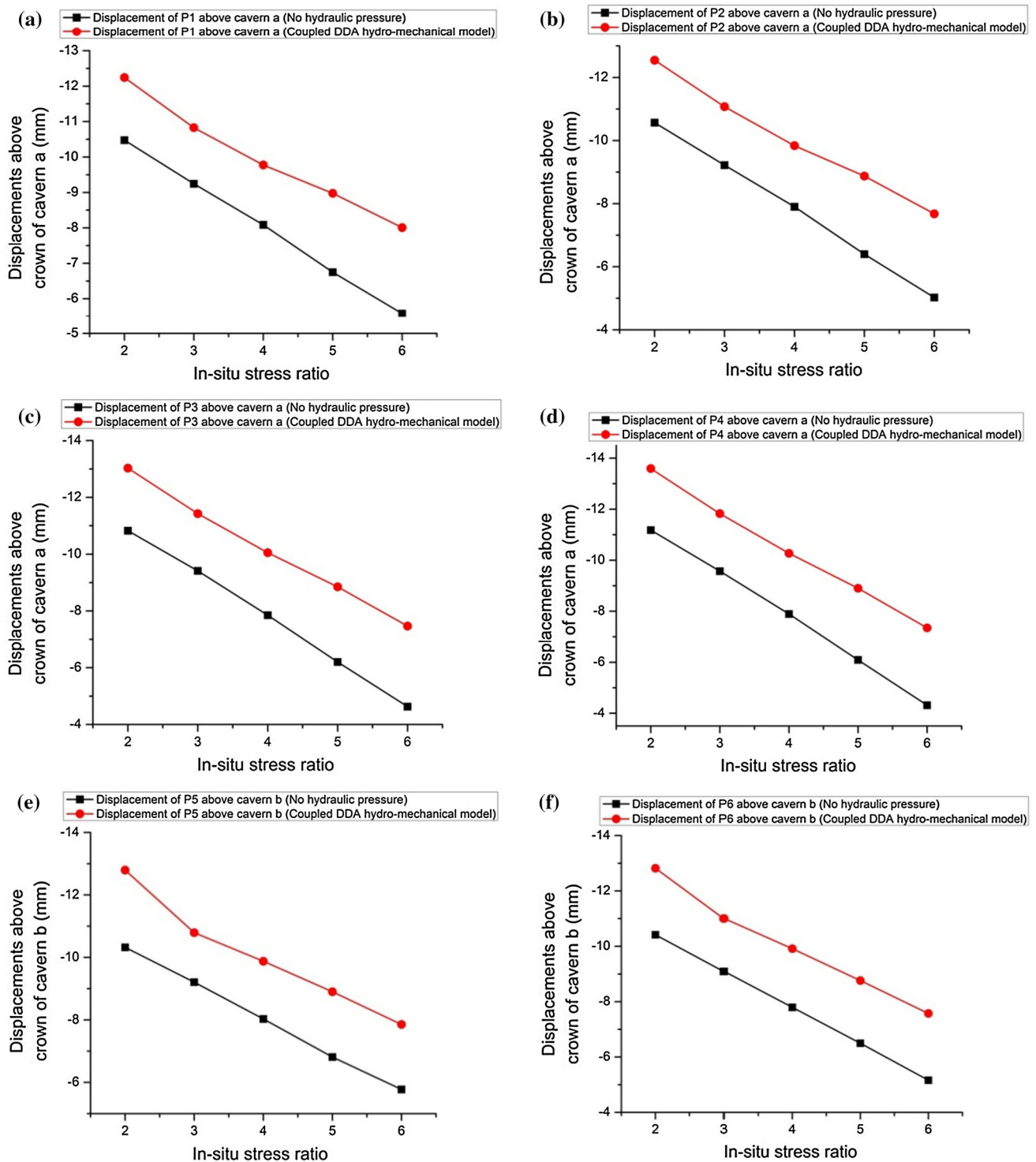


**Fig. 20** Comparison of the vertical displacements between the coupled DDA hydro-mechanical model and the original DDA without hydraulic pressure modeling for: **a** P1, **b** P2, **c** P3, **d** P4, **e** P5, **f** P6, **g** P7, and **h** P8

pressure. As the in situ stress ratio is increased gradually, the difference between the displacements obtained by the two methods is even clearer for each checked point (Fig. 20). Therefore, the cavern stability is overestimated if

the hydraulic pressure is neglected in the structural stability analysis.

Among the three methods for considering the hydraulic influence, the cavern stability evaluated by the coupled



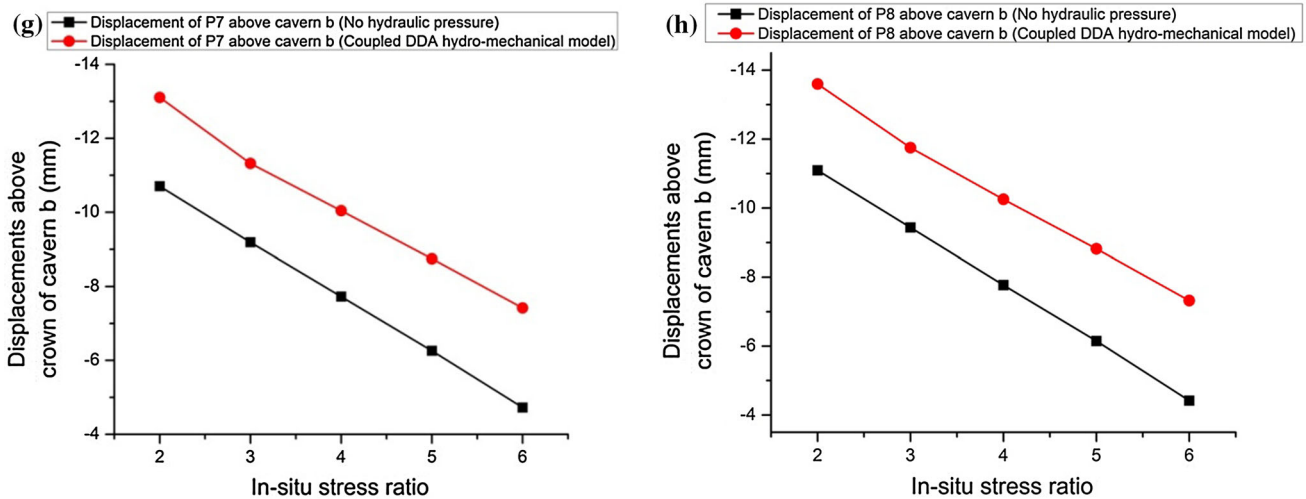


Fig. 20 continued

hydro-mechanical model is in the range of the results obtained by the other two methods. It suggests that the underground water should be modeled in a proper manner and that the coupled hydro-mechanical method is more suitable for predicting the inflow seepage rate and the stability of the underground structures.

## 4 Conclusions

The coupled hydro-mechanical model based on the discontinuous deformation analysis (DDA) method is developed in this paper, and the inflow rates and the vertical displacements above the cavern roofs are studied under five different in situ stress ratios. Also, the stability of the caverns is studied based on different joint spacings and joint dip angles, and under two different modeling methods for the hydraulic pressure. The numerical simulations indicate:

1. The total inflow rate drops as the in situ stress ratio increases, as the fracture aperture in the excavation zone decreases dramatically due to the increased effective stress. In addition, the vertical displacements above the cavern roofs also decrease when a higher in situ stress ratio is applied.
2. For the rock blocks located at Mode A (Fig. 7), the block size plays an important role in the displacement development of the rock blocks without the water pressure. But when the hydraulic pressure is considered, both the block size and the block shape can impact the displacement development for the rock blocks around the excavated boundary. In addition, the cavern stability is strongly related to the block shape (or block apex angle), shown in Case7080 and Case5085 around the cavern roof. Moreover, the

- results from Case5085 are in agreement with the failure mode description for the rock block in Mode B.
3. The coupled DDA hydro-mechanical model is more suitable for predicting the underground structural stability. If the static hydraulic pressure is used or the hydraulic pressure is neglected in the simulation, the results will be either underestimated or overestimated.

There are still some issues which need to be investigated further, including how the hydraulic conductivity is changed under the stress redistribution after the excavation, how partial failure of one cavern affects the stability of the adjacent cavern, and how the cavern failure develops based on different joint dip angles. All those issues are under investigation and the results will be reported in a future study.

## References

- Brady BHG, Brown ET (2004) Rock mechanics for underground mining, 3rd edn. Kluwer, Dordrecht
- Cammarata G, Fidelibus C, Cravero M, Barla G (2007) The hydro-mechanically coupled response of rock fractures. *Rock Mech Rock Eng* 40:41–61
- Chen G, Jia ZH, Ke JC (1997) Probabilistic analysis of underground excavation stability. *Int J Rock Mech Min Sci* 34:51.e1–51.e16
- Chen YF, Zhou CB, Sheng YQ (2007) Formulation of strain-dependent hydraulic conductivity for a fractured rock mass. *Int J Rock Mech Min Sci* 44:981–996
- Chen HM, Zhao ZY, Sun JP (2013) Coupled hydro-mechanical model for fractured rock masses using the discontinuous deformation analysis. *Tunn Undergr Space Technol* 38:506–516
- Esaki T, Du S, Mitani Y, Ikusada K, Jing L (1999) Development of a shear-flow test apparatus and determination of coupled properties for a single rock joint. *Int J Rock Mech Min Sci* 36:641–650
- Fernandez G, Moon J (2010a) Excavation-induced hydraulic conductivity reduction around a tunnel—Part 1: guideline for

- estimate of ground water inflow rate. *Tunn Undergr Space Technol* 25:560–566
- Fernandez G, Moon J (2010b) Excavation-induced hydraulic conductivity reduction around a tunnel—Part 2: verification of proposed method using numerical modeling. *Tunn Undergr Space Technol* 25:567–574
- Gale WJ, Blackwood RL (1987) Stress distributions and rock failure around coal mine roadways. *Int J Rock Mech Min Sci Geomech Abstr* 24:165–173
- Goodman RE, Shi GH (1985) *Block theory and its application to rock engineering*. Prentice-Hall, Englewood Cliffs, NJ, USA
- Hatzor YH, Arzi AA, Zaslavsky Y, Shapira A (2004) Dynamic stability analysis of jointed rock slopes using the DDA method: king Herod's Palace, Masada, Israel. *Int J Rock Mech Min Sci* 41:813–832
- Indraratna B, Wang JC (1996) Effect of stress change on water inflows to underground excavations. *Aust Geomechanics J* 29:99–114
- Ivars DM (2006) Water inflow into excavations in fractured rock—a three-dimensional hydro-mechanical numerical study. *Int J Rock Mech Min Sci* 43:705–725
- Jia P, Tang CA (2008) Numerical study on failure mechanism of tunnel in jointed rock mass. *Tunn Undergr Space Technol* 23:500–507
- Jing LR (2003) A review of techniques, advances and outstanding issues in numerical modelling for rock mechanics and rock engineering. *Int J Rock Mech Min Sci* 40:283–353
- Jing LR, Ma Y, Fang ZL (2001) Modeling of fluid flow and solid deformation for fractured rocks with discontinuous deformation analysis (DDA) method. *Int J Rock Mech Min Sci* 38:343–355
- Kinoshita N, Ishii T, Kuroda H, Tada H (1992) Prediction of permeability changes in an excavation response zone. *Nucl Eng Des* 138:217–224
- Ning YJ, Zhao ZY (2013) A detailed investigation of block dynamic sliding by the discontinuous deformation analysis. *Int J Numer Anal Meth Geomech* 37:2373–2393
- Ning YJ, Zhao ZY, Sun JP, Yuan WF (2012) Using the discontinuous deformation analysis to model wave propagations in jointed rock masses. *CEMS Comput Model Eng Sci* 89:221–262
- Rutqvist J, Stephansson O (2003) The role of hydromechanical coupling in fractured rock engineering. *Hydrogeol J* 11:7–40
- Shi GH (1988) *Discontinuous deformation analysis: a new numerical model for the statics and dynamics of block systems*. PhD dissertation, Department of Civil Engineering, University of California at Berkeley, Berkeley, CA
- Solak T (2009) Ground behavior evaluation for tunnels in blocky rock masses. *Tunn Undergr Space Technol* 24:323–330
- Solak T, Schubert W (2004) Influence of block size and shape on the deformation behavior and stress development around tunnels. Paper presented at the EUROCK 2004 and 53rd Geomechanics Colloquium, Salzburg, Austria, October 2004
- Sun JP, Zhao ZY (2010) Effects of anisotropic permeability of fractured rock masses on underground oil storage caverns. *Tunn Undergr Space Technol* 25:629–637
- Sun JP, Zhao ZY, Zhang Y (2011) Determination of three dimensional hydraulic conductivities using a combined analytical/neural network model. *Tunn Undergr Space Technol* 26:310–319
- Witherspoon PA, Wang JSY, Iwai K, Gale JE (1980) Validity of cubic law for fluid flow in a deformable rock fracture. *Water Resour Res* 16:1016–1024
- Yeung MR, Leong LL (1997) Effects of joint attributes on tunnel stability. *Int J Rock Mech Min Sci* 34:348.e1–348.e18
- Zhao EX, Gao JT (2009) Analysis of Mayazi tunnel excavation under considering the seepage field. *Geotech Eng Tech* 23:232–236 (in Chinese)
- Zhao J, Hefny AM, Zhou YX (2005) Hydrofracturing in situ stress measurements in Singapore granite. *Int J Rock Mech Min Sci* 42:577–583
- Zhu WS, Zhao J, Hudson JA (2004) *Stability analysis and modelling of underground excavations in fractured rocks*. Elsevier *Geo-Engineering Book Series*, vol 1, pp 67–87